batteries

Article

A SOH Estimation Method for Lithium-Ion Batteries Based on CPA and CNN-KAN

Kaixin Cheng [1], Chaolong Zhang [1,*], Kui Shao [2], Jin Tong [3], Anxiang Wang [1], Yujie Zhou [1], Zhao Zhang [1] and Yan Zhang [1]

[1] College of Intelligent Science and Control Engineering, Jinling Institute of Technology, Nanjing 211169, China; c17706238928@163.com (K.C.); 15005507945@163.com (A.W.); yujay_zhou@126.com (Y.Z.); zhang888@jit.edu.cn (Z.Z.); yan04749@jit.edu.cn (Y.Z.)
[2] School of Future Technology, China University of Geosciences, Wuhan 430074, China; 15720588750@163.com
[3] China Academy of Information and Communications Technology, Beijing 100088, China; tongjin@caict.ac.cn
* Correspondence: zhangchaolong@jit.edu.cn

Abstract

Lithium-ion batteries are the primary power source for new energy vehicles, making accurate estimation of their state of health (SOH) essential for ensuring the safe operation of battery systems. This paper proposes a Capacity–Power Analysis (CPA) method that incorporates temperature features to enhance feature extraction across a broader range. Additionally, we introduce an SOH estimation method for lithium batteries based on a Convolutional Neural Network (CNN) and a Kolmogorov–Arnold Network (KAN). By extracting the capacity–power curve and average temperature features during constant-current and constant-voltage charging, the CNN-KAN model establishes a nonlinear mapping relationship between the extracted features and SOH, enabling high-precision SOH estimation for lithium-ion batteries. Four 18650 batteries were tested under various charging and discharging conditions in a laboratory setting. The coefficient of determination (R^2) exceeded 96.4%, the root mean square error (RMSE) was below 0.86%, and the mean absolute error (MAE) was under 0.7%, confirming that the proposed method demonstrates excellent estimation performance.

Keywords: lithium-ion battery; state of health; Kolmogorov–Arnold network

check for updates

Academic Editor: Alessandro Lampasi

Received: 7 May 2025
Revised: 16 June 2025
Accepted: 18 June 2025
Published: 20 June 2025

Citation: Cheng, K.; Zhang, C.; Shao, K.; Tong, J.; Wang, A.; Zhou, Y.; Zhang, Z.; Zhang, Y. A SOH Estimation Method for Lithium-Ion Batteries Based on CPA and CNN-KAN. *Batteries* **2025**, *11*, 238. https://doi.org/10.3390/batteries11070238

Copyright: © 2025 by the authors. Licensee MDPI, Basel, Switzerland. This article is an open access article distributed under the terms and conditions of the Creative Commons Attribution (CC BY) license (https://creativecommons.org/licenses/by/4.0/).

1. Introduction

Lithium-ion batteries are widely used in new energy vehicles [1–3], smart grids, and energy storage systems [4] due to their numerous advantages, including high energy density [5], long cycle life [6], elevated operating voltage, and environmental sustainability [7]. However, during extended charge–discharge cycles, continuous irreversible physicochemical reactions within the battery can lead to performance degradation [8,9]. This degradation is primarily characterized by the persistent growth of the solid electrolyte interphase (SEI) and the loss of active lithium. It is essential to recognize that when this decline in performance reaches a critical threshold, it not only significantly reduces the battery's available capacity but also dramatically increases the risk of safety hazards, such as thermal runaway. Therefore, developing an accurate battery state of health (SOH) [10–12] estimation system has become a vital technical focus to ensure the safe operation of lithium battery systems and optimize their management.

At present, SOH estimation for lithium batteries is primarily categorized into three methods: direct measurement [13–15], model-based methods [16,17], and data-driven

methods [18–20]. For the direct measurement method, reference [13] proposed an in situ quantitative method for detecting irreversible lithium plating during the entire lifespan of lithium-ion batteries, which provides a possibility for the quantitative measurement and on-board detection of irreversible lithium plating; reference [14] systematically summarized the direct measurement method for the SOH of lithium batteries, and analyzed its applicability and challenges in the secondary utilization scenarios; reference [15] achieved direct and in situ measurement of lithium distribution in the graphite electrodes of lithium batteries using neutron imaging technology, providing an innovative method for SOH assessment. For the model-based methods, reference [16] implemented an online adaptive weight correction method based on an equivalent circuit model to update the weight–state of charge (SOC)–temperature relationship; reference [17] constructed a simple and robust capacity estimation model by using degradation patterns as bridging features, providing valuable references for the actual capacity estimation of battery packs. For data-driven methods, reference [18] proposed an efficient approach that integrates graph convolution and long short-term memory networks to accurately estimate the battery health status based on short-term charging data; reference [19] proposed an efficient method that combines synthetic data pre-training with real data transfer learning to quickly and accurately estimate the health status of in-service battery packs; reference [20] proposed a multi-task learning framework based on the Convolutional Neural Network–Multi-gate Mixture of Gated Recurrent Unit (CMMOG), which can handle multiple SOH estimation regression tasks simultaneously.

Common methods for the direct measurement of SOH in lithium batteries include ampere-hour integration, internal resistance measurement, and electrochemical impedance spectroscopy (EIS). The ampere-hour integration method [21] estimates the actual capacity of the battery by integrating the current over time during the battery's charging and discharging process, thereby assessing its SOH. The internal resistance measurement method [22] measures the internal resistance of the battery through pulse charging and discharging or direct current internal resistance testing, and calculates the SOH of the battery based on the change in internal resistance. The EIS method [23] applies multi-frequency sine wave signals to the battery, analyzes the changes in parameters such as the charge transfer resistance in the impedance spectrum, and thereby correlates the aging degree of the battery. Although this method is straightforward and intuitive, it is time-consuming. Currently, it is primarily suited for professional laboratory environments, which limits its application in practical settings.

Model-based methods can be categorized into two primary types: equivalent circuit models (ECM) and electrochemical models [24,25]. The equivalent circuit model constructs a network using traditional electrical components, such as resistors and capacitors, to simulate the aging behavior of batteries. In contrast, the electrochemical model employs differential equations to describe the dynamic processes of charge transfer, material diffusion, and reaction kinetics within the battery. For example, one study [26] achieved an accurate estimation of the SOH of lithium batteries by developing a coupling model that accounts for aging effects. Another study [27] completed SOH estimation of lithium batteries using a fractional-order RC circuit. Although model-based methods offer high parameter identifiability, they encounter challenges related to parameter sensitivity. When key parameters within the lithium-ion battery change, parameter identification must be redone, complicating the modeling process and significantly increasing computational costs.

The data-driven approach aims to establish the mapping relationship between SOH and characteristic parameters by analyzing battery operating data, without depending on complex electrochemical mechanism models [28,29]. Data-driven methods typically involve feature extraction and model construction. Current feature extraction technolo-

gies [30], which are based on voltage, current, and other parameters, can indicate observable performance changes; however, they do not provide a comprehensive explanation of the internal degradation mechanisms of the battery. Although Incremental Capacity Analysis (ICA) and Differential Voltage Analysis (DVA), which are based on mechanistic analysis, can reveal electrode material activity loss and lithium-ion migration mechanisms through voltage-capacity phase transition characteristics, these methods are only applicable during the constant current charging stage. This limitation arises because ICA and DVA rely on small voltage variations, which appear in the denominator for ICA and in the numerator for DVA. During the constant voltage charging stage, the voltage variation is zero, causing the ICA value to tend towards infinity and the DVA value to tend towards zero, rendering these methods infeasible for analysis at that stage. Furthermore, these methods are not compatible with constant-voltage phase feature extraction, and their characterization of power dynamic response characteristics is inadequate. Therefore, the Capacity–Power Analysis (CPA) method proposed in this study facilitates data acquisition and multi-dimensional feature extraction throughout the entire charging cycle, making it suitable for a wider range of operating conditions. The model construction methods include Back Propagation Neural Network (BPNN) [31,32], Support Vector Machine (SVM) [33], Random Forest (RF) [34], Long Short-Term Memory (LSTM) [35,36], Gated Recurrent Unit (GRU) [37], and Transformer [38], among others. Traditional models often rely on indirect posterior analysis methods, which can render their decision-making logic difficult to interpret intuitively, resulting in poor model interpretability. In contrast, the Kolmogorov–Arnold Network (KAN) model converts high-dimensional feature mapping into a combination of univariate functions, thereby enhancing interpretability. As research has advanced, scholars have introduced fusion models [39], such as Convolutional Neural Network (CNN)-LSTM and CNN-GRU, which effectively address the limitations of individual models in SOH estimation. These fusion models not only tackle the complexities of dynamic time series modeling but also capture the long-term dependencies associated with battery aging through their deep network architectures.

In this paper, a new framework for estimating the SOH of lithium-ion batteries is proposed. Firstly, in terms of feature extraction, the charging capacity–power (CP) curve is analyzed to extract the CP features, and these features are integrated with the average operating temperature (AOT) features of the battery to form multi-dimensional features. Subsequently, a highly accurate SOH estimation model is constructed using the CNN-KAN model.

The contributions of this paper are outlined as follows:

(1) In the realm of feature extraction, this paper introduces a multi-dimensional feature that integrates temperature and CP. Traditional Incremental Capacity (IC) [40] and Differential Voltage (DV) [41] curves frequently omit data segments with constant voltage during the analysis of charging data, resulting in the loss of valuable information. The CPA method addresses this pre-processing loss by directly examining the dynamic changes in capacity and power throughout the charging process. Furthermore, by incorporating temperature characteristics that are closely associated with battery aging, this approach optimizes the utilization of charging data;

(2) This study presents an innovative CNN-KAN fusion model that achieves significant advancements in various aspects by harnessing the local feature extraction capabilities of CNN and the nonlinear modeling advantages of KAN. Specifically, the CNN module effectively captures essential trend features within the multi-feature sequence while simultaneously reducing data dimensions. By employing a mathematical representation theory, the KAN layer transforms high-dimensional feature mappings

into a combination of univariate functions with strong interpretability, thereby greatly enhancing the model's overall interpretability.

2. Lithium Battery SOH

The *SOH* of lithium-ion batteries can be defined through multiple dimensions such as capacity, internal resistance, cycle count, and energy efficiency. Among these definition methods, capacity attenuation can most directly reflect the aging degree of lithium batteries. It not only determines the battery's endurance time and available energy, but also has the advantages of being universal and not being limited by the battery's chemical system. In contrast, when using the internal resistance method to define the *SOH*, the internal resistance value of the battery is easily affected by temperature, and there is no strict corresponding relationship between it and capacity attenuation. The cycle number rule is not precise enough as it cannot distinguish the actual aging degree under different stress conditions and cannot reflect sudden aging problems in real time. The energy efficiency rule has strict requirements for measurement accuracy. Based on the above analysis, considering that the capacity definition method has significant advantages such as simplicity and accuracy, this paper will mainly define the *SOH* of lithium batteries from the perspective of capacity, as illustrated in Equation (1):

$$SOH = \frac{C_{presented\ capacity}}{C_{initial\ capacity}} \times 100\% \tag{1}$$

where $C_{presented\ capacity}$ refers to the available capacity of the current lithium battery, while $C_{initial\ capacity}$ denotes the rated capacity of the lithium battery.

3. Feature Correlation Analysis and Selection

Compared to traditional ICA and DVA methods, the CPA method proposed in this paper can achieve feature extraction across the entire charging range and effectively represent power variations within the features.

3.1. CPA

CPA is a method used to evaluate battery performance by analyzing the relationship between capacity and power during the battery charging process. The definition is provided in Equation (2):

$$CP = \frac{dQ}{dP} \tag{2}$$

where Q represents battery capacity and P denotes battery power. Figure 1 illustrates the *CP* curve of a single cycle of an individual battery, with the blue curve depicting the measured data and the red curve representing the Gaussian-filtered result.

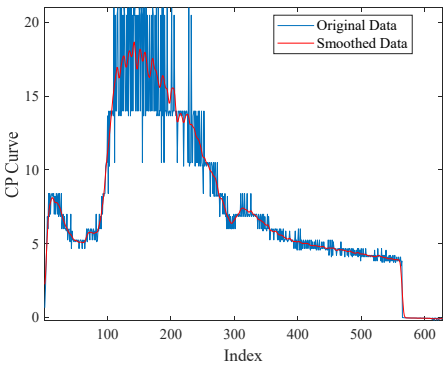


Figure 1. Single-cycle CP curve.

As shown in Equation (3), the area of the *CP* curve can be calculated by the following expression:

$$CP_\text{area} = \int_a^b \left(\frac{dQ}{dP}\right)_i di \tag{3}$$

where i is the data point index, $\left(\frac{dQ}{dP}\right)_i$ is the *CP* value of the ith data point, and $[a,b]$ is the integration interval. Figure 2 illustrates the variation in the *CP* integral area throughout the cycle of a single battery under laboratory conditions.

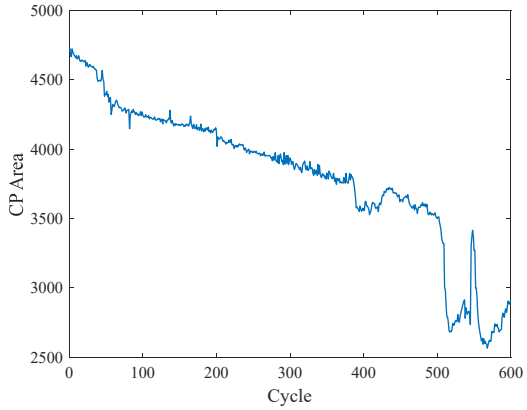


Figure 2. CP area variation diagram of single battery.

As shown in Equation (4), the *peak* value of the *CP* curve can be calculated by the following expression:

$$CP_peak = (\frac{dQ}{dP})max \tag{4}$$

where Q represents the battery capacity and P denotes the battery power. Figure 3 illustrates the variation in the *peak CP* curve throughout the cycle of a single battery under laboratory conditions. The blue curve depicts the measured data, while the orange curve represents the Gaussian-filtered result.

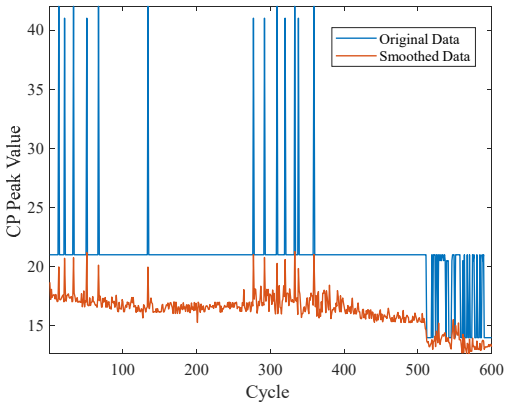


Figure 3. CP peak value variation diagram of single battery.

3.2. AOT

Temperature is the primary factor influencing the aging process of lithium batteries [42–44]. Elevated temperatures accelerate the decomposition of the electrolyte, leading to the thickening of the SEI film and the inactivation of active materials due to phase transitions. Conversely, low temperatures promote the growth of lithium dendrites, which can result in irreversible capacity loss and pose safety risks. The *AOT* metric reflects the long-term thermal environment of the

battery and serves as a crucial indicator for estimating the extent of battery aging. The definition is provided in Equation (5):

$$AOT = \frac{1}{n}\sum_{i=1}^{n} T_i \tag{5}$$

where T_i is the temperature value of the i time sampling in the cycle, and n is the total number of temperature data sampling in the cycle. Figure 4 illustrates the variation in AOT in a single battery as the number of cycles increases.

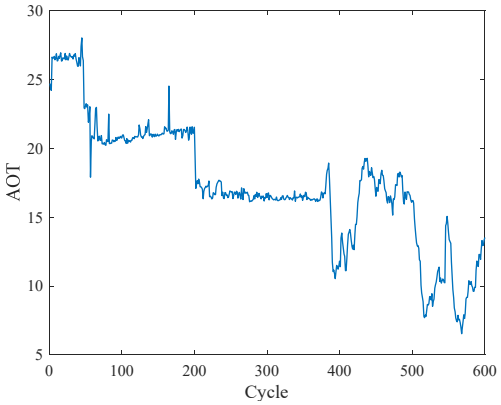


Figure 4. AOT value variation diagram of single battery.

3.3. ICA

ICA is a battery SOH assessment method based on electrochemical characteristics. It characterizes the aging mechanism of the battery by quantifying the differential response of capacity to voltage in the charging and discharging curves. The definition is provided in Equation (6):

$$\begin{aligned} IC &= \frac{dQ}{dV} \\ IC_peak &= (\frac{dQ}{dV})max \\ IC_\text{area} &= \int_a^b \left(\frac{dQ}{dV}\right) dV \end{aligned} \tag{6}$$

where Q represents the battery capacity, V represents the battery voltage, and a and b are the integral intervals for selecting the voltage. Figures 5 and 6 show the changes in the integral area and *peak* value of *IC* for a single battery throughout the entire cycling process under laboratory conditions. Figure 5 presents the variation in *IC* integral area throughout the cycle of a single battery under laboratory conditions, while Figure 6 demonstrates the corresponding changes in *IC peak* values.

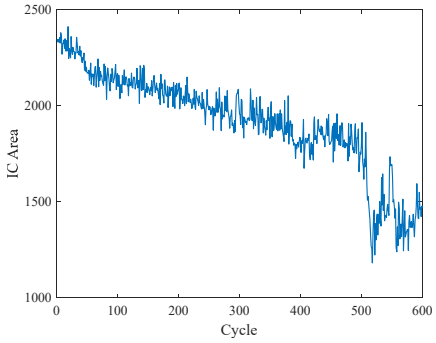


Figure 5. IC area variation diagram of single battery.

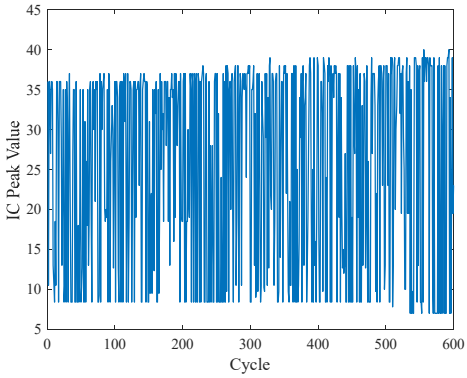


Figure 6. IC peak value variation diagram of single battery.

3.4. DVA

DVA is a battery SOH evaluation method based on electrochemical characteristics. It characterizes the aging mechanisms of the battery by quantifying the differential response of voltage to capacity in the charging and discharging curves. The definition is provided in Equation (7):

$$\begin{aligned} DV &= \frac{dV}{dQ} \\ DV_peak &= (\frac{dV}{dQ})max \end{aligned} \tag{7}$$

where V represents the battery voltage, and Q represents the battery capacity. Figure 7 demonstrates the corresponding changes in DV peak values.

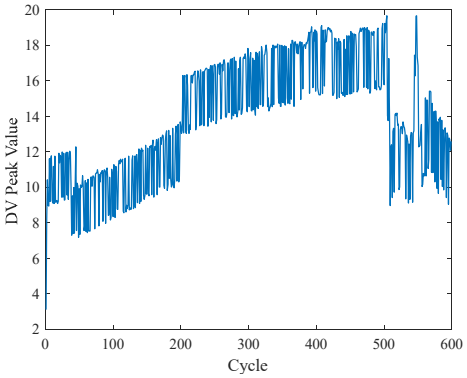


Figure 7. DV peak value variation diagram of single battery.

3.5. Pearson Correlation Coefficient

The Pearson correlation coefficient is a statistical measure that quantifies the degree of linear correlation between two continuous variables. Its values range from -1 to 1 and are defined as the ratio of the covariance to the product of the standard deviations. This definition is presented in Equation (8) below.

$$r = \frac{\sum_{i=1}^{n}(x_i - \overline{x})(y_i - \overline{y})}{\sqrt{\sum_{i=1}^{n}(x_i - \overline{x})^2} \cdot \sqrt{\sum_{i=1}^{n}(y_i - \overline{y})^2}} \tag{8}$$

where x_i and y_i are the values of the two variables of the i-th sample, $\overline{x}$ and $\overline{y}$ are the mean values of the two variables, and n is the number of samples.

In order to quantify the linear correlation between each feature and battery SOH, the Pearson correlation coefficient was utilized for the statistical analysis of the aforementioned features. The results are presented in Table 1.

Table 1. Pearson correlation coefficients of each feature.

Pearson Correlation Coefficient					
IC Area	CP Area	CP Peak	IC Peak	AOT	DV Peak
0.9676	0.9887	0.8019	−0.0362	0.9137	−0.1825

The Pearson correlation coefficient is used to quantify the degree of linear association between two variables, and its value ranges from −1 to 1. The magnitude of the absolute value of this coefficient directly reflects the strength of the correlation, while the sign indicates the direction of the correlation. Specifically, when the correlation coefficient approaches 1, it indicates that the two variables show a significant upward trend, that is, when one variable increases, the other variable also increases accordingly; when the correlation coefficient approaches −1, it shows that the two variables have a significant inverse relationship, that is, an increase in one variable is accompanied by a decrease in the other variable; if the correlation coefficient is close to 0, it means that there is no significant linear correlation between the two variables. In the IC curve, the IC Area can effectively represent the loss of lithium inventory or the total degradation of active materials, and thus has a strong correlation of 0.9676 with the battery SOH; but the IC Peak is susceptible to noise and charging–discharging rates, and its correlation is only −0.0362. The peak of the DV curve is sensitive to interface by-products, but the battery capacity is mainly determined by the loss of interstitial lithium, so the correlation between DV Peak and SOH is only −0.1825. AOT is closely related to the aging trend of the battery through influencing thermodynamic and reaction kinetic processes. During the experiment, the seasonal temperature drop is synchronized with the SOH decay, resulting in a correlation coefficient of 0.9137 between the two. In addition, the CP curve proposed in this paper directly reflects the capacity–power coupling characteristics during the charging process, avoiding the loss of information from voltage pre-treatment, and thus CP Area and CP Peak show high correlations of 0.9887 and 0.8019, respectively.

Although traditional methods can effectively characterize the performance state of a battery by extracting statistical characteristics from voltage, current, and time series data, they often lack a comprehensive understanding of the underlying attenuation mechanisms. While ICA and DVA methods can elucidate battery aging at a mechanistic level, their reliance on voltage fluctuations in charging data limits data utilization and complicates feature extraction across a wide range of operating conditions. Therefore, this paper proposes the development of a multi-feature system that utilizes CP Area as the core feature, in conjunction with the AOT feature. Notably, the temperature characteristics provide valuable insights into the battery aging process across multiple physical domains, significantly enhancing the SOH estimation of lithium batteries.

4. The CNN-KAN Model

4.1. Convolutional Neural Network

In traditional fully connected neural networks, each neuron is connected to every node in the preceding layer. This architecture leads to a significant increase in the number of parameters as the number of network layers or data dimensions increases. Such a structure complicates the training process, raises computational costs, and impedes the extraction of local features from high-dimensional data, such as images, ultimately degrading model performance.

A CNN [45] is a deep learning model specifically designed for processing grid-like data. It utilizes structures such as convolutional layers and pooling layers to capture local features, allowing the model to comprehend complex patterns through a layer-by-layer

abstraction. This architecture makes CNNs particularly effective for tasks such as image classification, object detection, and semantic segmentation, and it also extends to fields like natural language processing and time series analysis. Figure 8 illustrates the structural diagram of a CNN.

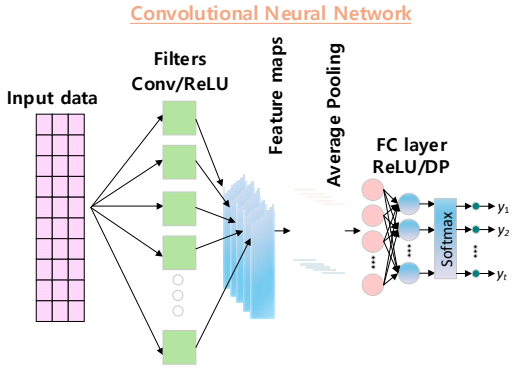


Figure 8. CNN structure diagram.

The core of a CNN is the convolution operation, which is mathematically expressed in Equation (9):

$$Z_{i,j,k} = \sum_{m=0}^{M-1} \sum_{n=0}^{N-1} \sum_{c=0}^{C-1} W_{m,n,c,k} \cdot X_{i+m,j+n,c} + b_k \tag{9}$$

where $Z_{i,j,k}$ represents the output feature graphs. $X_{i+m,j+n,c}$ denotes the pixel value of the c-th channel in the input feature map at the spatial position $(i + m, j + n)$, where (i,j) are the current coordinates of the output feature map, (m,n) indicates the relative shift within the convolution kernel, and c is the index of the input channel. $W_{m,n,c,k}$ represents the weight parameters of the k-th convolution kernel at position (m,n) in input channel c, with a convolution kernel size of $M \times N$. b_k is the bias term associated with the k-th filter. In this paper, the original two-dimensional input features are mapped to an eight-dimensional feature space through a convolutional layer. Subsequently, a 1×1 convolution is employed to generate spatial attention weights. After normalization, the original features are weighted to enhance the key features.

4.2. KAN Model

The KAN model [46,47] aims to address complex multivariate continuous functions by utilizing combinations of univariate functions. Unlike traditional multilayer perceptrons, the KAN model replaces the fixed activation function in the network with a learnable univariate function. This approach offers distinct advantages in terms of parameter efficiency, interpretability, and nonlinear fitting capability. Figure 9 below illustrates the structural diagram of the KAN model.

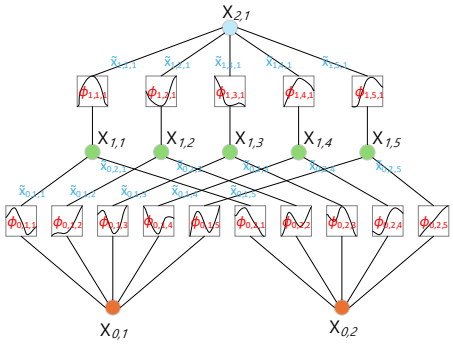


Figure 9. KAN structure diagram.

KAN's core equation is derived from the Kolmogorov–Arnold Representation Theorem, as illustrated in Equation (10). For any multivariable continuous function f: $R^n \rightarrow R$, there exists a set of one-dimensional continuous functions Φ_i and Ψ_{ij},

$$f(x_1, x_2, \ldots, x_n) = \sum_{i=1}^{2n+1} \phi_i \left(\sum_{j=1}^{n} \psi_{ij}(x_j) \right) \tag{10}$$

where Ψ_{ij} is a set of nonlinear transformation functions (mapping input variables), and Φ_i is a set of weighted summation transformation functions (mapping to the final output).

The core architecture of the KAN model in this paper consists of three main levels:

(1) Adaptive grid construction: its core Equation (11) is shown as follows:

$$\begin{gathered} G = \epsilon \cdot G_{uniform} + (1 - \epsilon) \cdot G_{adaptive} \\ G \in \mathbb{R}^{d \times (K+2m+1)} \end{gathered} \tag{11}$$

where G is the adaptive grid, ϵ is the uniform grid mixed weight (default: 0.02), $G_{uniform}$ is the uniform interval grid, $G_{adaptive}$ is the adaptive grid generated based on data quantiles, d is the input feature dimension, K is the number of basic grid points, and m is the B-spline order.

In the KAN layer, grid G serves as the core component, facilitating the adaptive nonlinear transformation of input features. The grid independently generates non-uniformly distributed nodes for each input dimension and dynamically adjusts node density to accommodate changes in characteristics: sparse nodes are allocated to features with gradual temperature variations, while dense nodes are assigned to abrupt changes in CP features. The B-spline basis function derived from G is combined with learnable weights to nonlinearly map 8-dimensional input features to a 16-dimensional space.

(2) B-spline basis function calculation: its core Equation (12) is shown as follows:

$$B_{i,j,k}^{p}(x) = \frac{x_i^{(j)} - G_{j,k}}{G_{j,k+p} - G_{j,k}} B_{i,j,k}^{p-1}(x) + \frac{G_{j,k+p+1} - x_i^{(j)}}{G_{j,k+p+1} - G_{j,k+1}} B_{i,j,k+1}^{p-1}(x) \tag{12}$$

where $B^{p}{}_{i,j,k}$ is the p-order value of the i-th sample, the j-th dimensional feature, and the k-th basis function; $x^{(j)}{}_i$ is the j-th dimensional input feature of the i-th sample; $G_{j,k}$ is the k-th grid node of the j-th dimensional feature; and p is the B-spline order—for example, $p = 3$ is the cubic spline.

The distribution of B-spline basis functions is dynamically regulated by an adaptive grid G, which allows the grid nodes to automatically align with the statistical characteristics of the input features. This approach enables each feature dimension to independently learn the most suitable nonlinear transformation rules, thereby facilitating adaptive nonlinear modeling based on the distribution characteristics of the various features discussed in this paper.

(3) Spline coefficient fitting: the core Equation (13) is shown as follows:

$$W = \underset{W}{\operatorname{argmin}} \|BW - Y\|_2^2 + \lambda \|W\|_2^2 \tag{13}$$

where W is the trainable spline coefficient matrix, B is the B-spline basis function matrix, Y is the training target output, and λ is the L2 regularization coefficient.

Spline coefficient fitting enables the transformation from an 8-dimensional feature space to a 16-dimensional nonlinear feature space. The process begins by calculating the corresponding B-spline basis function values for each input dimension, which are then

linearly combined with the trained weight matrix W. In this procedure, each submatrix of the W matrix governs the nonlinear transformation rules for a specific input dimension, ensuring that each dimension of the resulting 16-dimensional feature is a weighted fusion of the original eight features after undergoing independent nonlinear transformations. These extended features are ultimately integrated through a fully connected layer to produce accurate SOH estimates.

4.3. CNN-KAN Model

In this paper, we propose a SOH estimation method for lithium batteries based on the CNN-KAN model. The model first extracts local spatiotemporal features from the charging curve using a CNN and employs an attention mechanism to enhance the recognition of key patterns. Subsequently, a KAN layer is introduced to replace the traditional fully connected network. This layer facilitates nonlinear mapping from an 8-dimensional feature space to a 16-dimensional space through the use of adaptive grids and B-spline transformations, ultimately yielding accurate SOH estimation results. In the task of estimating the SOH of batteries, different model architectures exhibit significant performance differences. The CNN module, with its unique convolutional kernel structure, can efficiently automatically extract multi-scale spatial features from battery time-series data, and simultaneously achieve intelligent data dimension compression through pooling layers, while significantly reducing computational complexity while retaining key information. In contrast, traditional time-series models have obvious limitations: LSTM, although good at capturing long-term dependencies, has high computational complexity and suffers from the problem of gradient vanishing; GRU models, although simplifying the gating structure, are more sensitive to high-frequency noise; and Transformer models, although performing well in large-scale data scenarios, the experimental data scale in this study is far from meeting their optimal performance requirements. It is worth noting that the performance of the SVR model highly depends on the empirical selection of the kernel function, which brings significant uncertainty in practical applications. The KAN module adopted in this study demonstrates unique advantages: Firstly, by replacing the traditional fixed activation function with a learnable activation function, this model can more accurately model the complex nonlinear relationships in the battery aging process. Secondly, the KAN model has stronger interpretability. These characteristics enable KAN to exhibit outstanding performance in the battery SOH estimation task. CNN-KAN architecture effectively combines the advantages of local feature extraction provided by the CNN with the efficient nonlinear modeling capabilities of the KAN. Figure 10 illustrates the flowchart of the CNN-KAN model.

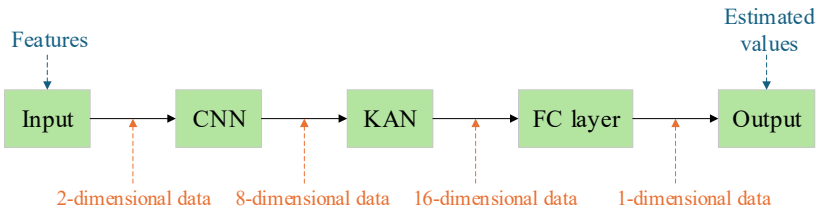


Figure 10. CNN-KAN flowchart.

5. Experimental Procedure, Results, and Analysis

5.1. Experimental Data

The aging data for the Lishen 18650 single lithium battery, collected from 16 August 2023 to 26 June 2024, were used as the experimental data. The nominal capacity and voltage of each lithium battery are 2.5 Ah and 3.6 V, respectively.

Through the high-performance battery testing system established in the laboratory, we conducted aging experiments on lithium-ion batteries at room temperature and collected relevant aging data. The high-performance battery testing system comprises the Neware BTS-4000 (NEWARE, Shenzhen, China) single battery testing equipment and a host computer. The single battery testing equipment, renowned for its high responsiveness, precision, and efficiency, supports constant current, constant voltage, and combined constant current and constant voltage test modes. It is capable of performing cycle life and pulse power tests. The host computer is used to set test parameters and to collect and store data. The experimental setup is illustrated in Figure 11.

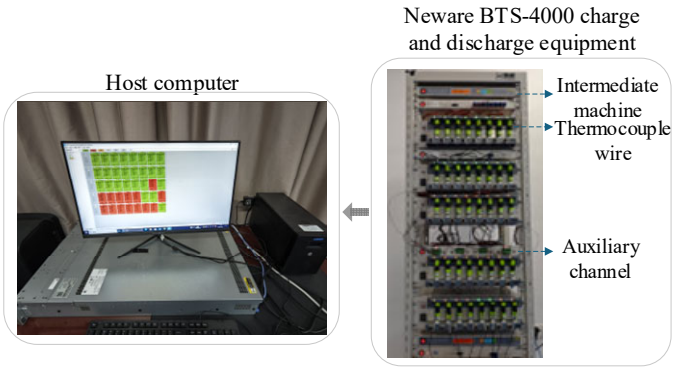


Figure 11. Experimental setup.

In this experiment, four individual lithium batteries (labeled 1–4) were selected for aging tests at charging rates of 0.2 C, 0.3 C, 0.4 C, and 0.6 C, respectively. First, each battery is charged using a constant current at the specified rates until the voltage reaches 4.2 V. The charging process then continues in constant-voltage mode at 4.2 V until the charging current decreases to 0.02 C, at which point charging is halted. Once charging is complete, the battery undergoes a constant discharge until the voltage drops to 3 V.

The detailed parameters of the lithium-ion battery are shown in Table 2 below.

Table 2. The detailed parameters of the lithium-ion single-cell batteries that participated in this experiment.

Cathode	$LiFePO_4$
Anode	Graphite
Rated capacity	2.5 Ah
Nominal voltage	3.6 V
Discharge rate	2600 mA
Charging cutoff current	50 mA

The SOH changes of four batteries are illustrated in Figure 12. Notably, the atypical SOH rebound phenomenon observed in Batteries 1 and 2 can be attributed to the significant influence of AOT.

The lithium battery capacity recovery phenomenon refers to the temporary increase in capacity that occurs during the cycling or standing process of the battery. Its essence stems from the brief restoration of the reversible degradation mechanism within the battery. In this study, batteries 1–4 were tested using charging rates of 0.2 C, 0.3 C, 0.4 C, and 0.6 C, respectively. Due to the differences in charging rates, the charging time of batteries 1 and 2 was significantly longer than that of batteries 3 and 4, and they experienced a longer operating time under the same number of cycles. When the environmental temperature experienced seasonal cooling to 10 degrees Celsius and then warmed up, this temperature recovery had a significant activating effect on batteries 1 and 2: the increase

in temperature promoted the re-infiltration process of the electrolyte in the electrode pores, accelerated the reactivation and dissolution of dead lithium, and improved the self-repairing kinetics characteristics of the SEI membrane. In contrast, the temperature of batteries 3 and 4 basically remained at around 15 degrees Celsius throughout the latter part of the experiment, with Battery 3 experiencing only a slight temperature recovery, while Battery 4 did not undergo a temperature recovery process at all. Therefore, Battery 3 only exhibited a slight capacity recovery phenomenon at the end of the cycle, while Battery 4 did not show capacity recovery phenomenon. Figure 13 shows the variation curves of each battery's AOT with the number of cycles. Since the characteristics of this study include AOT, it is possible to enhance the estimation accuracy of SOH through the collaborative effect of multiple physical domains.

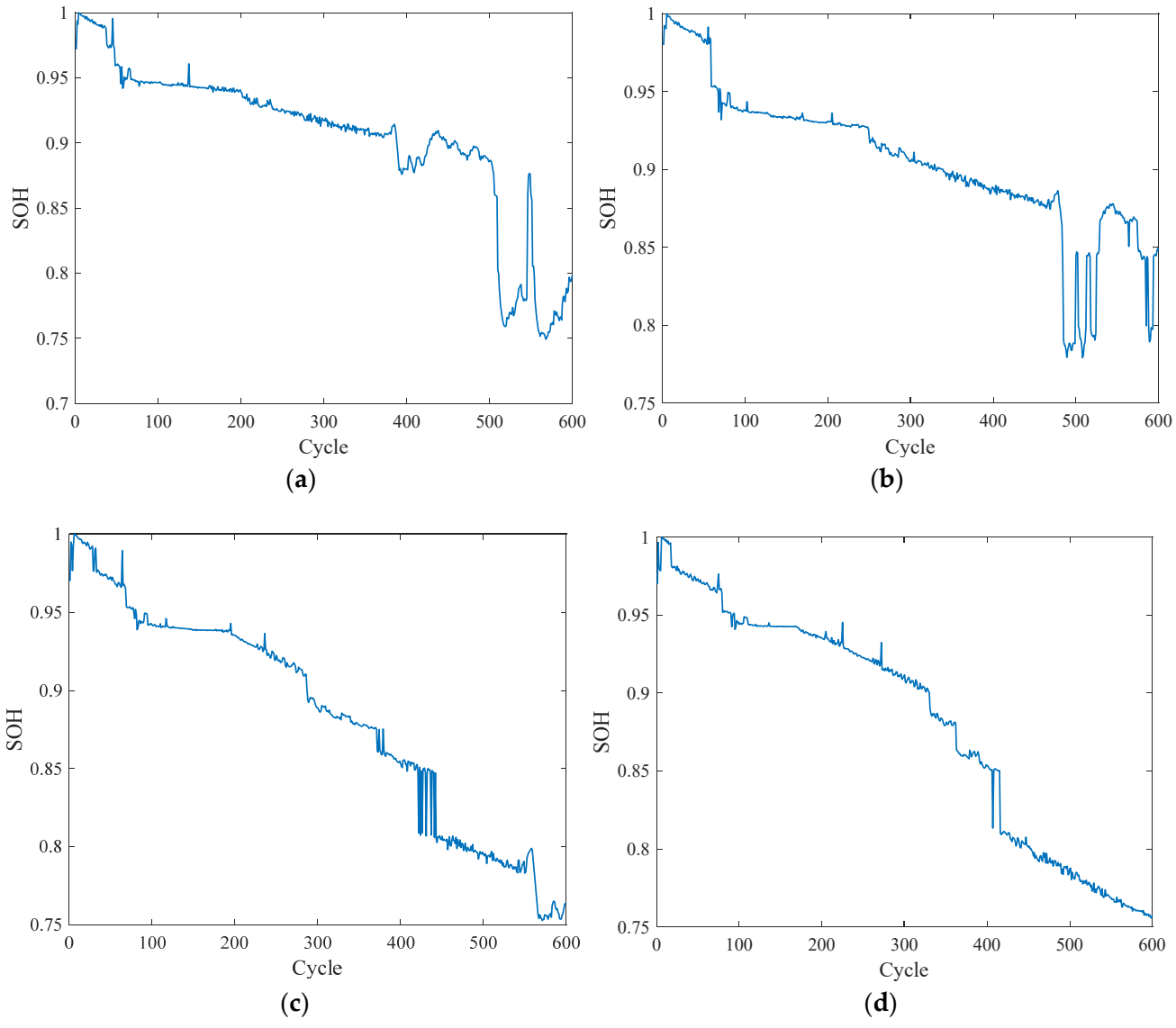


Figure 12. The lithium-ion battery SOH deterioration trend for (**a**) Battery 1, (**b**) Battery 2, (**c**) Battery 3, and (**d**) Battery 4.

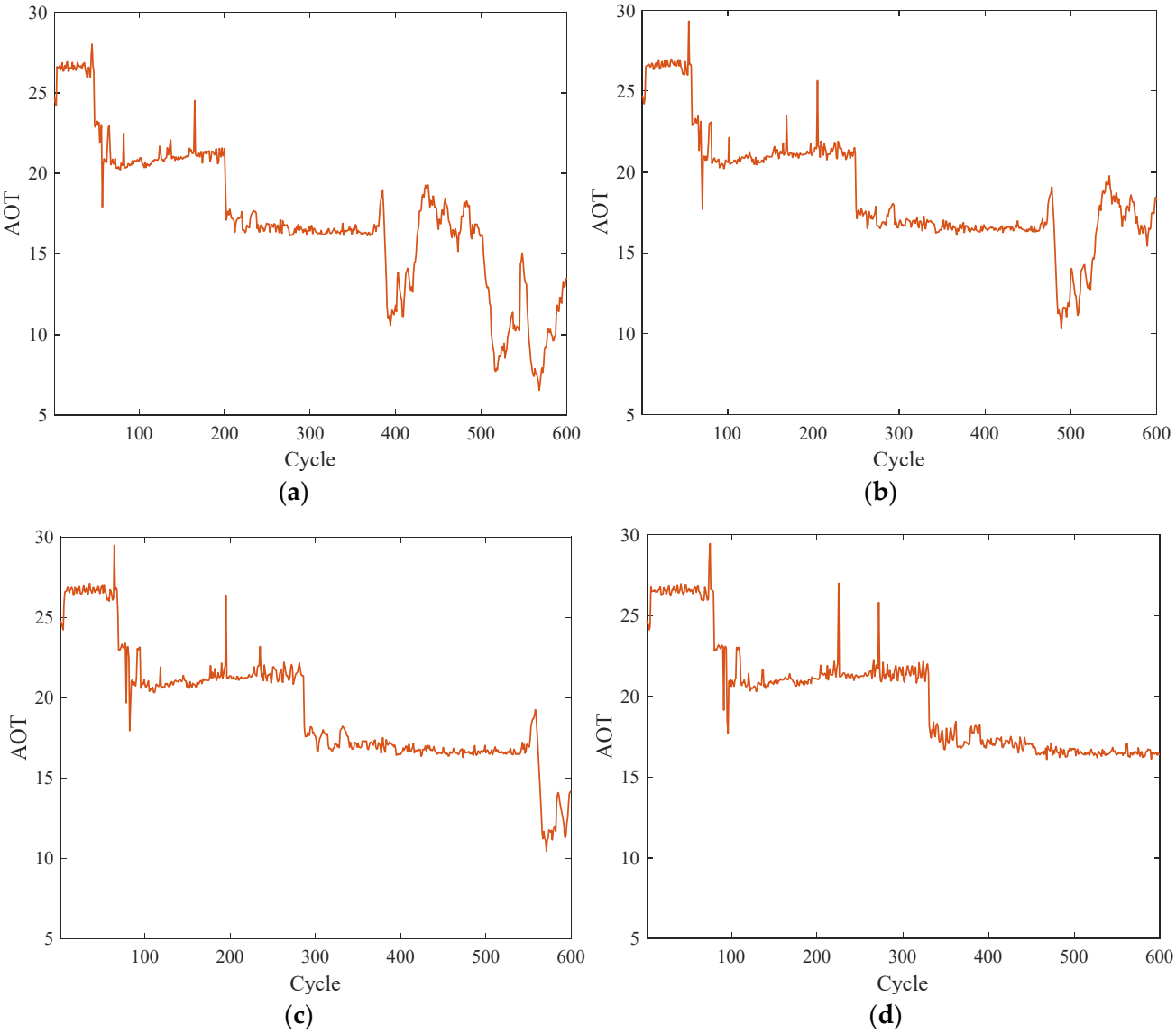


Figure 13. Variation of AOT in lithium-ion batteries for (**a**) Battery 1, (**b**) Battery 2, (**c**) Battery 3, and (**d**) Battery 4.

5.2. Experimental Procedure

The specific steps for estimating the SOH of a lithium battery are as follows:

Step 1 Measurement of power, capacity, and temperature during the constant current-constant voltage charging phase.

Step 2 The CPA area, AOT, and SOH for each charging stage are calculated, resulting in the generation of a processed dataset.

Step 3 The processed dataset is divided into a training set and a test set, with each set receiving 50% of the total data.

Step 4 Training data and CNN-KAN method were used to establish the SOH estimation model.

Step 5 The trained SOH estimation model was employed to evaluate the test data of lithium batteries, thereby validating the model's performance and estimation accuracy.

The specific experimental process is shown in Figure 14 below.

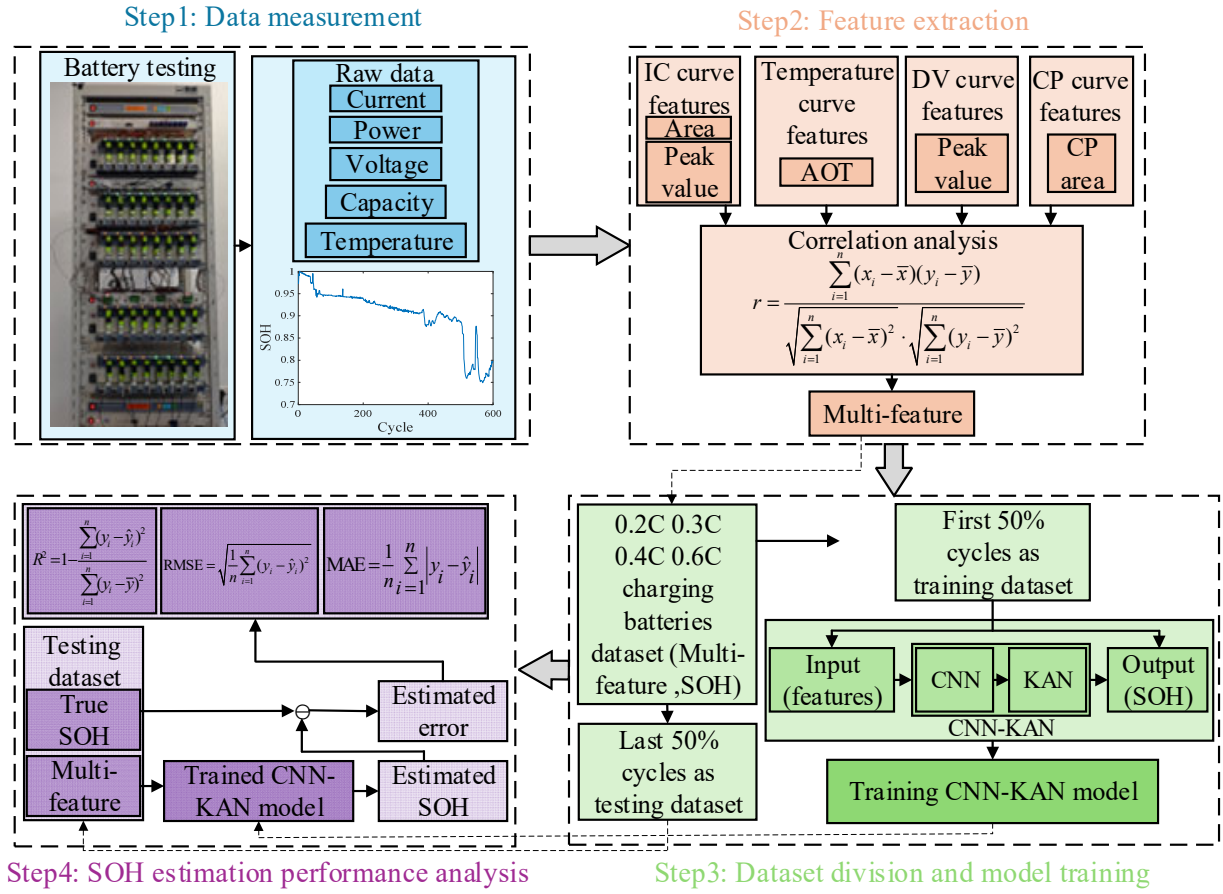


Figure 14. Specific experimental process.

5.3. Experimental Results and Analysis

In this experiment, R^2, RMSE, and MAE were used as metrics to evaluate the accuracy of the prediction results. The equations for their calculation, labeled as (14) to (16), are presented below:

$$R^2 = 1 - \frac{\sum_{i=1}^{n} (y_i - \hat{y}_i)^2}{\sum_{i=1}^{n} (y_i - \overline{y})^2} \tag{14}$$

$$\mathrm{RMSE} = \sqrt{\frac{1}{n}\sum_{i=1}^{n} (y_i - \hat{y}_i)^2} \tag{15}$$

$$\mathrm{MAE} = \frac{1}{n}\sum_{i=1}^{n} |y_i - \hat{y}_i| \tag{16}$$

where n represents the number of charge and discharge cycles, y_i is the true value of SOH, $\overline{y}$ is the mean value of the true value, and $\hat{y}_i$ is the estimated value of SOH. Model evaluation index analysis indicates that a smaller RMSE value corresponds to higher accuracy. Furthermore, the closer the R^2 value is to 1, the greater the model's explanatory power. A reduction in MAE signifies a concentration of errors.

5.3.1. Feature Extraction

In this paper, the CP area is used as the key characteristic parameter. Figure 15 shows the variation trends of the CP area across the cycles of the other three batteries, excluding the sample shown in Figure 2.

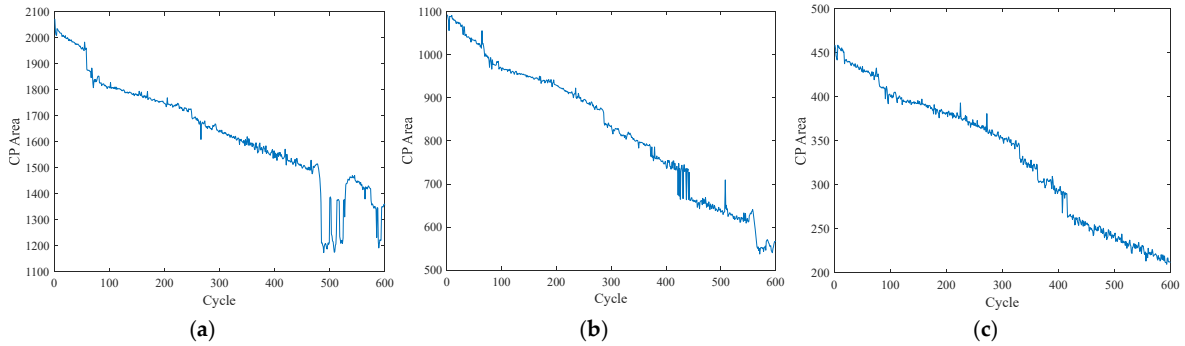


Figure 15. The lithium-ion battery CP Area deterioration trend for (**a**) Battery 2, (**b**) Battery 3, and (**c**) Battery 4.

5.3.2. SOH Estimation Results, Comparative Experiments and Analysis

This paper proposes a SOH estimation method for lithium batteries based on the CNN-KAN architecture, which integrates the area under the CP curve and the AOT characteristics for modeling. Figure 16 presents the SOH estimation results for four batteries.

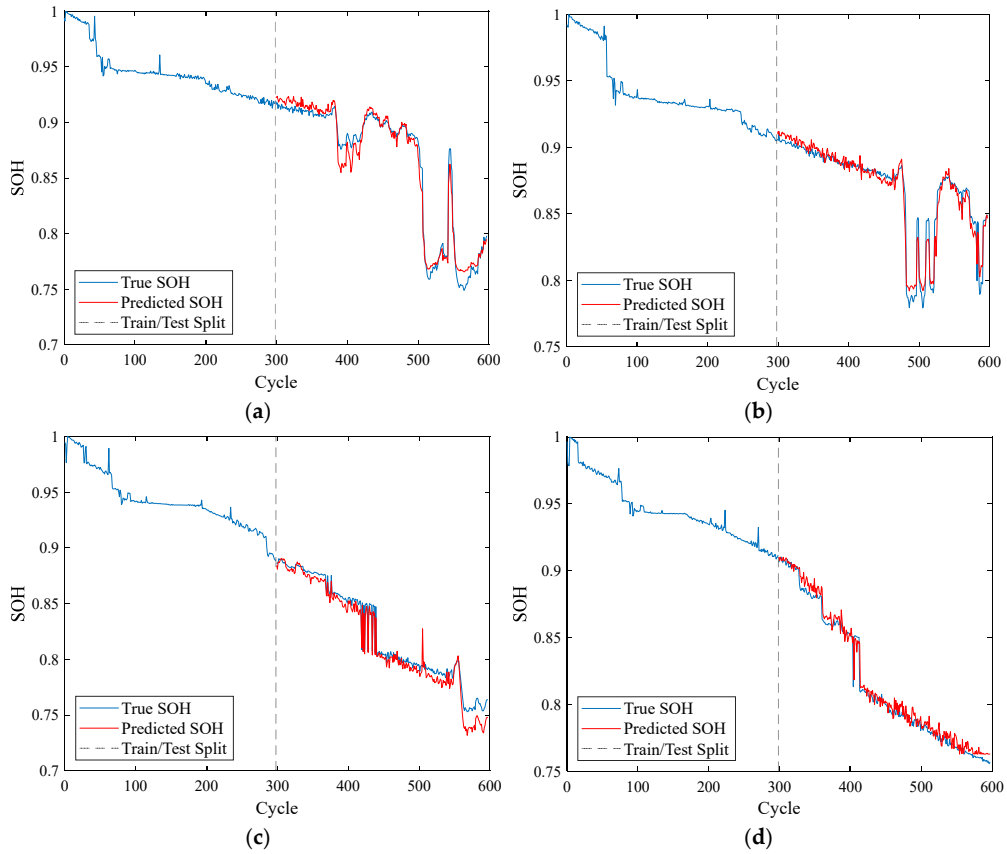


Figure 16. The lithium-ion battery SOH estimation for (**a**) Battery 1, (**b**) Battery 2, (**c**) Battery 3, and (**d**) Battery 4.

To verify the stability and generalizability of the proposed SOH estimation method, comparative experiments were conducted on batteries 1 through 4 from two perspectives: model and features. For the algorithm comparison, commonly used SOH estimation algorithms, as listed in Table 3, were employed for testing. The test results are presented in Figure 17, while the performance indicators are detailed in Table 4. Regarding the comparison of input variables, various feature combinations outlined in Table 5 were

selected as model inputs for SOH estimation. The estimated results are illustrated in Figure 18, and the corresponding performance indicators are provided in Table 6.

Table 3. Common algorithms.

Method	Input	Estimation Algorithm
Proposed method	CP Area, AOT	CNN-KAN
Comparative method-1	CP Area, AOT	CNN-LSTM
Comparative method-2	CP Area, AOT	CNN-GRU
Comparative method-3	CP Area, AOT	CNN-Transformer
Comparative method-4	CP Area, AOT	CNN-SVR

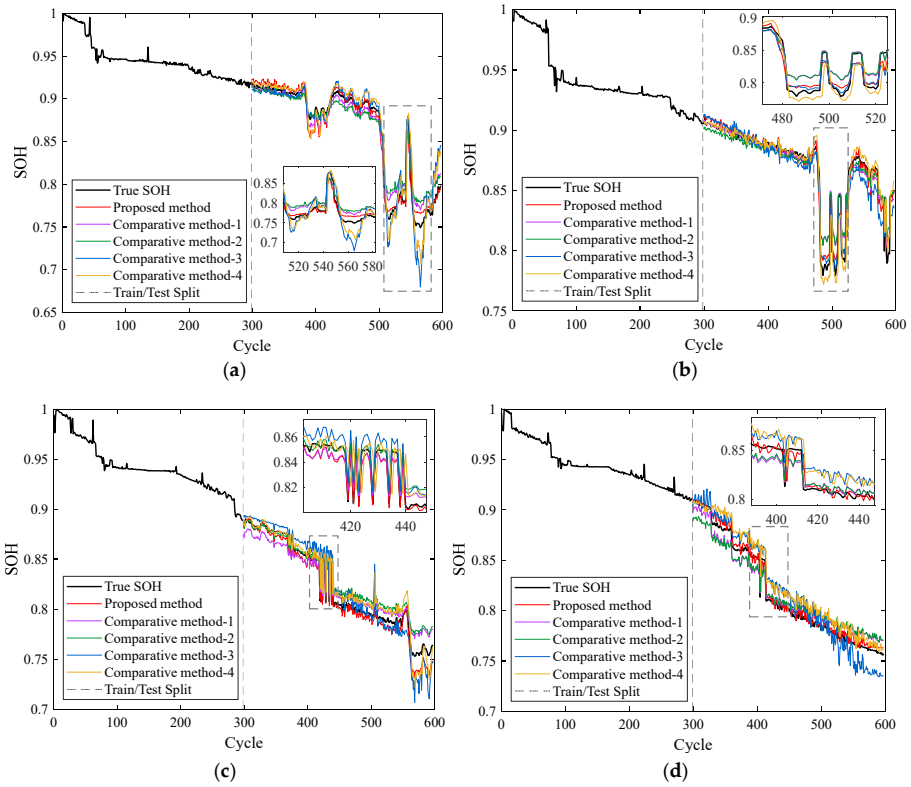


Figure 17. Comparison of common lithium-ion battery algorithms for (**a**) Battery 1, (**b**) Battery 2, (**c**) Battery 3, and (**d**) Battery 4.

Table 4. Performance indicators of common algorithms.

Method	Evaluation Metric (%)	Battery-1	Battery-2	Battery-3	Battery-4
Proposed method	R^2	97.88	96.44	96.56	98.34
	RMSE	0.85	0.65	0.81	0.63
	MAE	0.66	0.49	0.62	0.46
Comparative method-1	R^2	95.51	94.00	93.93	95.50
	RMSE	1.24	0.84	1.07	1.04
	MAE	1.02	0.53	0.97	0.95
Comparative method-2	R^2	94.29	93.04	92.47	93.98
	RMSE	1.40	0.91	1.19	1.20
	MAE	1.11	0.63	0.92	1.12
Comparative method-3	R^2	92.81	91.40	91.27	91.36
	RMSE	1.57	1.01	1.28	1.44
	MAE	1.00	0.81	1.01	1.25
Comparative method-4	R^2	93.50	92.04	91.37	91.81
	RMSE	1.49	0.97	1.28	1.40
	MAE	1.06	0.55	0.91	1.23

Table 5. Contrast of features.

Feature	Input	Estimation Algorithm
Proposed feature	CP Area, AOT	CNN-KAN
Comparative feature-1	IC Area	CNN-KAN
Comparative feature-2	AOT	CNN-KAN
Comparative feature-3	IC Area, AOT	CNN-KAN
Comparative feature-4	CP Area	CNN-KAN
Comparative feature-5	CP Area, IC Area	CNN-KAN

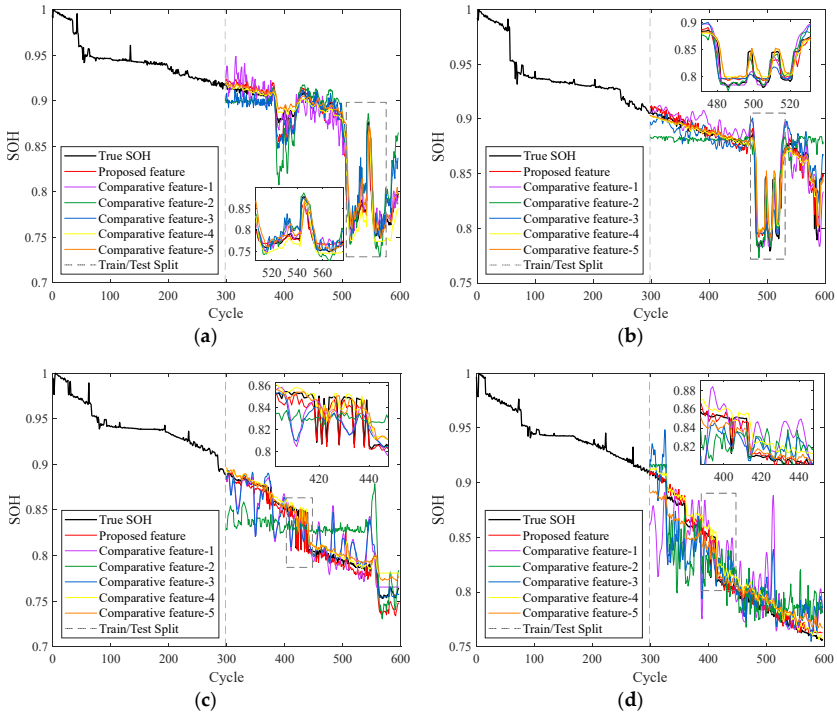


Figure 18. Comparison of lithium-ion battery characteristics for (**a**) Battery 1, (**b**) Battery 2, (**c**) Battery 3, and (**d**) Battery 4.

Table 6. Performance indicators for features comparison.

Feature	Evaluation Metric (%)	Battery-1	Battery-2	Battery-3	Battery-4
Proposed feature	R^2	97.88	96.44	96.56	98.34
	RMSE	0.85	0.65	0.81	0.63
	MAE	0.66	0.49	0.62	0.46
Comparative feature-1	R^2	94.79	84.43	80.47	61.53
	RMSE	1.33	1.36	1.92	3.04
	MAE	1.02	1.02	1.43	2.21
Comparative feature-2	R^2	84.60	67.66	40.74	74.71
	RMSE	2.29	1.96	3.35	2.46
	MAE	1.71	1.32	3.06	1.97
Comparative feature-3	R^2	92.48	86.17	81.88	78.48
	RMSE	1.60	1.28	1.85	2.27
	MAE	1.22	0.89	1.32	1.76
Comparative feature-4	R^2	97.05	93.91	94.18	95.81
	RMSE	1.00	0.85	1.05	1.00
	MAE	0.67	0.51	0.74	0.84
Comparative feature-5	R^2	95.50	93.51	94.15	94.65
	RMSE	1.24	0.88	1.05	1.13
	MAE	0.72	0.49	0.77	1.03

The experimental results demonstrate that the CNN-KAN model proposed in this study offers significant advantages in estimating the SOH of lithium batteries. As illustrated in Figure 17 and Table 4, this model achieved the highest performance across four battery tests, with R^2 values of 97.88%, 96.44%, 96.56%, and 98.34%, respectively. This represents an average improvement of 2.57 percentage points over the second-best CNN-LSTM model. In terms of error metrics, the RMSE and MAE of the CNN-KAN model remained at the lowest levels, decreasing by an average of 0.311% compared to the CNN-LSTM model. Comparative model performance analysis revealed that the CNN-LSTM achieved commendable results in sequence modeling, with an average R^2 of 94.73%. It also demonstrated the best performance in the Battery-2 test, as indicated by its RMSE. Conversely, the CNN-GRU exhibited significant fluctuations during the Battery-4 test, with the MAE rising to 1.12%. The R^2 of the CNN-Transformer decreased to 91.27% in the Battery-3 test, primarily due to computational complexity. The CNN-SVR recorded an RMSE exceeding 1.40% in both the Battery-1 and Battery-4 tests, which can be attributed to the limitations of its fixed kernel function. Notably, all comparative models performed relatively poorly in the Battery-3 test, with the R^2 fluctuations of the CNN-SVR being the most pronounced. In contrast, the CNN-KAN maintained an R^2 value of 96.56% in the Battery-3 test, which is 2.63 percentage points higher than the best-performing comparative model, thereby highlighting the advantages of this model.

Through a comparative analysis of input characteristics, we found that the Pearson correlation coefficients for the IC peak, CP peak, and DV peak are relatively low. Based on these analysis results, this study ultimately selected the IC area, AOT, and their combined features as the comparison features, systematically comparing them with the features proposed in this paper. Detailed comparisons and combinations of features are presented in Table 5.

The experimental results indicate that the fusion features of CP Area and AOT proposed in this paper demonstrate significant advantages in SOH estimation. As shown in Table 6, this combination of features achieved the best performance across the four groups of battery tests. The R^2 consistently remained within a high range of 96.44% to 98.34%, representing an average increase of 2.07 percentage points compared to the second-best combination of CP Area. Additionally, the RMSE and MAE metrics were significantly superior to those of other feature combinations, with RMSE being 1.02% lower than that of the IC Area and AOT combination, and MAE being 0.74% lower. The analysis reveals that when the AOT feature is used in isolation, the model's performance is the least satisfactory due to the weak correlation between temperature and SOH. Although the IC Area feature performs relatively well, its R^2 value fluctuates between 94.79% and 61.53%, making it challenging to fully capture the complex degradation process of the battery. When using the CP Area feature alone, the model performs quite well. However, due to the lack of the temperature characteristic, which has an impact on batteries, there is still a certain gap compared to the proposed optimal combination. In contrast, the integration of CP Area and AOT features creates a more comprehensive characterization system for battery aging. This system captures the dynamic coupling characteristics of capacity and power during charging while also incorporating temperature, a critical influencing factor. This combination of features not only provides more detailed degradation information but also establishes a more reliable foundation for accurate estimates of SOH.

6. Conclusions

This study proposes a lithium-ion battery SOH estimation method based on the fusion features of CP Area and AOT and the CNN-KAN hybrid model. Compared with traditional ICA and DVA methods, although they can explain the battery aging behavior from the

electrochemical mechanism perspective, their dependence on voltage change values leads to low data utilization. The CPA method adopted in this study achieves effective feature extraction within a wide operating range by analyzing the coupling relationship between capacity and power during charging, significantly improving data utilization. At the same time, the AOT features are combined to characterize the battery aging process from multiple physical domains. The feature fusion of these two methods establishes a more reliable feature basis for lithium-ion battery SOH estimation. In terms of the model architecture, the CNN-KAN hybrid model designed in this study, the CNN module can automatically extract multi-scale spatial features from the battery time series data through its unique convolution kernel structure, and achieve intelligent data dimension compression through the pooling layer, ensuring the integrity of key information while effectively reducing computational complexity. The KAN module adopts learnable adaptive activation functions instead of traditional fixed activation functions, which not only can more accurately model the complex nonlinear relationships in the battery aging process, but also has stronger model interpretability. Experimental verification shows that this method performs excellently in SOH estimation accuracy, with an R^2 value exceeding 96.4%, RMSE controlled within 0.86%, and MAE lower than 0.7%, fully demonstrating the effectiveness and reliability of the proposed method.

This study conducted tests based on laboratory measurements of Lishen 18650 single batteries. Although four battery samples were used for verification at different charging rates, the sources and diversity of the current dataset remain limited. Future work will expand to include data from actual operating conditions of electric vehicle battery packs and energy storage power stations to further validate the engineering applicability of the proposed method.

Author Contributions: Conceptualization, C.Z., Y.Z. (Yan Zhang) and K.C.; methodology, K.S.; software, K.C.; validation, C.Z., K.C. and Z.Z.; formal analysis, K.S.; investigation, Y.Z. (Yan Zhang), C.Z., K.C., J.T. and Z.Z.; resources, C.Z.; data curation, K.C. and A.W.; writing—original draft preparation, K.C.; writing—review and editing, K.C.; visualization, K.C.; supervision, C.Z.; project administration, K.S., A.W., Y.Z. (Yujie Zhou), J.T. and Z.Z.; funding acquisition, C.Z. All authors have read and agreed to the published version of the manuscript.

Funding: This work was supported by the major project of basic science (natural science) research in colleges and universities of Jiangsu Province under Grant No. 23KJA480002; "Qinglan Project" for universities in Jiangsu Province; scientific research foundation for high-level personnel in Jinling Institute of Technology under Grant No. jit-rcyj-202202.

Data Availability Statement: Data is contained within the article.

Conflicts of Interest: The authors declare no conflicts of interest.

References

1. Zhang, C.; Wang, J.; Zhang, L.; Zhang, W.; Zhu, T.; Yang, X.-G.; Cruden, A. Decoding battery aging in fast-charging electric vehicles: An advanced SOH estimation framework using real-world field data. *Energy Storage Mater.* **2025**, *78*, 104236. [CrossRef]
2. Xiong, R.; Wang, P.; Jia, Y.; Shen, W.; Sun, F. Multi-factor aging in Lithium Iron phosphate batteries: Mechanisms and insights. *Appl. Energy* **2025**, *382*, 125250. [CrossRef]
3. Deng, Z.; Xu, L.; Liu, H.; Hu, X.; Duan, Z.; Xu, Y. Prognostics of battery capacity based on charging data and data-driven methods for on-road vehicles. *Appl. Energy* **2023**, *339*, 120954. [CrossRef]
4. Meng, J.; Yang, F.; Peng, J.; Gao, F. A proximal policy optimization based control framework for flexible battery energy storage system. *IEEE Trans. Energy Convers.* **2024**, *39*, 1183–1191. [CrossRef]
5. Liu, Y.; Jiang, W.; Zhang, C.; Jia, P.; Zhang, Z.; Zheng, Y.; Yan, K.; Wang, J.; Qian, Y.; Guo, J.; et al. Realizing Environmentally Scalable Pre-Lithiation via Protective Coating of LiSi Alloys to Promote High-Energy-Density Lithium-Ion Batteries. *Inorganics* **2025**, *13*, 115. [CrossRef]

6. Zhu, J.; Xu, W.; Knapp, M.; Darma, M.S.; Mereacre, L.; Su, P.; Hua, W.; Liu-Théato, X.; Dai, H.; Wei, X.; et al. A method to prolong lithium-ion battery life during the full life cycle. Cell Rep. *Phys. Sci.* **2023**, *4*, 101464.
7. Lai, X.; Chen, J.; Chen, Q.; Han, X.; Lu, L.; Dai, H.; Zheng, Y. Comprehensive assessment of carbon emissions and environmental impacts of sodium-ion batteries and lithium-ion batteries at the manufacturing stage. *J. Clean. Prod.* **2023**, *423*, 138674. [CrossRef]
8. Wang, J.; Zhang, C.; Zhang, L.; Su, X.; Zhang, W.; Li, X.; Du, J. A novel aging characteristics-based feature engineering for battery state of health estimation. *Energy* **2023**, *273*, 127169. [CrossRef]
9. Zhang, C.; Zhao, S.; Yang, Z.; He, Y. A multi-fault diagnosis method for lithium-ion battery pack using curvilinear Manhattan distance evaluation and voltage difference analysis. *J. Energy Storage* **2023**, *67*, 107575. [CrossRef]
10. Qian, G.; Zheng, Y.; Li, X.; Sun, Y.; Han, X.; Ouyang, M. State of health estimation for lithium-ion batteries using impedance-based simplified timescale information. *Appl. Energy* **2025**, *382*, 125272. [CrossRef]
11. Xiong, X.; Wang, Y.; Li, K.; Chen, Z. State of health estimation for lithium-ion batteries using Gaussian process regression-based data reconstruction method during random charging process. *J. Energy Storage* **2023**, *72*, 108390. [CrossRef]
12. Che, Y.; Zheng, Y.; Onori, S.; Hu, X.; Teodorescu, R. Increasing generalization capability of battery health estimation using continual learning. *Cell Rep. Phys. Sci.* **2023**, *4*, 101743. [CrossRef]
13. You, H.; Jiang, B.; Zhu, J.; Wang, X.; Shi, G.; Han, G.; Wei, X.; Dai, H. In-situ quantitative detection of irreversible lithium plating within full-lifespan of lithium-ion batteries. *J. Power Sources* **2023**, *564*, 232892. [CrossRef]
14. Vignesh, S.; Che, H.S.; Selvaraj, J.; Tey, K.S.; Lee, J.W.; Shareef, H.; Errouissi, R. State of Health (SoH) estimation methods for second life lithium-ion battery—Review and challenges. *Appl. Energy* **2024**, *369*, 123542.
15. Owejan, J.P.; Gagliardo, J.J.; Harris, S.J.; Wang, H.; Hussey, D.S.; Jacobson, D.L. Direct measurement of lithium transport in graphite electrodes using neutrons. *Electrochim. Acta* **2012**, *66*, 94–99. [CrossRef]
16. Tang, A.; Huang, Y.; Liu, S.; Yu, Q.; Shen, W.; Xiong, R. A novel lithium-ion battery state of charge estimation method based on the fusion of neural network and equivalent circuit models. *Appl. Energy* **2023**, *348*, 121578. [CrossRef]
17. Feng, X.; Zhang, Y. Enhancing interpretability in data-driven battery capacity estimation through degradation mode analysis. *J. Power Sources* **2025**, *642*, 236938. [CrossRef]
18. He, Y.; Deng, Z.; Chen, J.; Li, W.; Zhou, J.; Xiang, F.; Hu, X. State-of-health estimation for fast-charging lithium-ion batteries based on a short charge curve using graph convolutional and long short-term memory networks. *J. Energy Chem.* **2024**, *98*, 1–11. [CrossRef]
19. Deng, Z.; Xu, L.; Liu, H.; Hu, X.; Wang, B.; Zhou, J. Rapid health estimation of in-service battery packs based on limited labels and domain adaptation. *J. Energy Chem.* **2024**, *89*, 345–354. [CrossRef]
20. Zhang, C.; Tu, L.; Yang, Z.; Du, B.; Zhou, Z.; Wu, J.; Chen, L. A CMMOG-based lithium-battery SOH estimation method using multi-task learning framework. *J. Energy Storage* **2025**, *107*, 114884. [CrossRef]
21. Fahmy, H.M.; Hasanien, H.M.; Alsaleh, I.; Ji, H.; Alassaf, A. State of health estimation of lithium-ion battery using dual adaptive unscented Kalman filter and Coulomb counting approach. *J. Energy Storage* **2024**, *88*, 111557. [CrossRef]
22. Lin, M.; Yan, C.; Wang, W.; Dong, G.; Meng, J.; Wu, J. A data-driven approach for estimating state-of-health of lithium-ion batteries considering internal resistance. *Energy* **2023**, *277*, 127675. [CrossRef]
23. Li, Y.; Maleki, M.; Banitaan, S. State of health estimation of lithium-ion batteries using EIS measurement and transfer learning. *J. Energy Storage* **2023**, *73*, 109185. [CrossRef]
24. Tong, Z.; Lv, C.; Bai, G.-D.; Yin, Z.-W.; Zhou, Y.; Li, J.-T. A review on applications and challenges of carbon nanotubes in lithium-ion battery. *Carbon Energy* **2025**, *7*, e643. [CrossRef]
25. Ni, Y.; Song, K.; Pei, L.; Li, X.; Wang, T.; Zhang, H.; Zhu, C.; Xu, J. State-of-health estimation and knee point identification of lithium-ion battery based on data-driven and mechanism model. *Appl. Energy* **2025**, *385*, 125539. [CrossRef]
26. Fang, D.; Wu, W.; Li, J.; Yuan, W.; Liu, T.; Dai, C.; Wang, Z.; Zhao, M. Performance simulation method and state of health estimation for lithium-ion batteries based on aging-effect coupling model. *Green Energy Intell. Transp.* **2023**, *2*, 100082. [CrossRef]
27. Chen, L.; Xie, S.; Lopes, A.M.; Li, H.; Bao, X.; Zhang, C.; Li, P. A new SOH estimation method for Lithium-ion batteries based on model-data-fusion. *Energy* **2024**, *286*, 129597. [CrossRef]
28. Fan, C.; Liu, K.; Ren, Y.; Peng, Q. Characterization and identification towards dynamic-based electrical modeling of lithium-ion batteries. *J. Energy Chem.* **2024**, *92*, 738–758. [CrossRef]
29. Fan, C.; Zhang, K.; Peng, Q.; Tian, J.; Liu, K.; Chung, C.Y. Fast Characterization of Lithium-Ion Battery Impedance and Nonlinearity Using Optimized Multisine Perturbation Signal. *IEEE Trans. Ind. Electron.* **2025**, 1–11. [CrossRef]
30. Li, X.; Lyu, M.; Li, K.; Gao, X.; Liu, C.; Zhang, Z. Lithium-ion battery state of health estimation based on multi-source health indicators extraction and sparse Bayesian learning. *Energy.* **2023**, *282*, 128445. [CrossRef]
31. Zhang, F.; Xing, Z.-X.; Wu, M.-H. State of health estimation for Li-ion battery using characteristic voltage intervals and genetic algorithm optimized back propagation neural network. *J. Energy Storage* **2023**, *57*, 106277.
32. Wu, M.; Zhong, Y.; Wu, J.; Wang, Y.; Wang, L. State of health estimation of the lithium-ion power battery based on the principal component analysis-particle swarm optimization-back propagation neural network. *Energy* **2023**, *283*, 129061. [CrossRef]

33. Li, Y.; Ye, M.; Wang, Q.; Lian, G.; Xia, B. An improved model combining machine learning and Kalman filtering architecture for state of charge estimation of lithium-ion batteries. *Green Energy Intell. Transp.* **2024**, *3*, 100163. [CrossRef]
34. Sulaiman, M.H.; Mustaffa, Z. State of charge estimation for electric vehicles using random forest. *Green Energy Intell. Transp.* **2024**, *3*, 100177. [CrossRef]
35. Zhang, C.; Luo, L.; Yang, Z.; Du, B.; Zhou, Z.; Wu, J.; Chen, L. Flexible method for estimating the state of health of lithium-ion batteries using partial charging segments. *Energy* **2024**, *295*, 131009. [CrossRef]
36. Li, C.; Zhu, S.; Zhang, L.; Liu, X.; Li, M.; Zhou, H.; Zhang, Q.; Rao, Z. State of charge estimation of lithium-ion battery based on state of temperature estimation using weight clustered-convolutional neural network-long short-term memory. *Green Energy Intell. Transp.* **2025**, *4*, 100226. [CrossRef]
37. Zhang, C.; Luo, L.; Yang, Z.; Zhao, S.; He, Y.; Wang, X.; Wang, H. Battery SOH estimation method based on gradual decreasing current, double correlation analysis and GRU. *Green Energy Intell. Transp.* **2023**, *2*, 100108. [CrossRef]
38. Xu, R.; Wang, Y.; Chen, Z. A hybrid approach to predict battery health combined with attention-based transformer and online correction. *J. Energy Storage* **2023**, *65*, 107365. [CrossRef]
39. Bao, X.; Chen, L.; Lopes, A.M.; Li, X.; Xie, S.; Li, P.; Chen, Y. Hybrid deep neural network with dimension attention for state-of-health estimation of Lithium-ion Batteries. *Energy* **2023**, *278*, 127734. [CrossRef]
40. Wang, T.; Zhu, Y.; Zhang, Z.; Bi, F.; Sun, L.; Kim, T.; Shang, Y. A SOH estimation method within micro-voltage interval based on ICA peak distribution for lithium-ion batteries. *IEEE Trans. Transp. Electrif.* **2025**. [CrossRef]
41. Xu, W.; Zhu, J.; Zhang, J.; Tian, M.; Cai, J.; Wu, H.; Wei, G.; Chen, T.; Wei, X.; Dai, H. Investigation of lithium-ion battery degradation by corrected differential voltage analysis based on reference electrode. *Appl. Energy* **2025**, *389*, 125735. [CrossRef]
42. Wang, Y.; Feng, X.; Guo, D.; Hsu, H.; Hou, J.; Zhang, F.; Xu, C.; Chen, X.; Wang, L.; Zhang, Q.; et al. Temperature excavation to boost machine learning battery thermochemical predictions. *Joule* **2024**, *8*, 2639–2651. [CrossRef]
43. Shang, Y.; Chen, G.; Peng, Q.; Zhu, T.; Liu, K. An intelligent preheating approach based on high-gain control for lithium-ion batteries in extremely cold environment. *IEEE Trans. Ind. Electron.* **2024**, *71*, 4697–4706. [CrossRef]
44. Sun, Y.; Xie, H.; Diao, Q.; Xu, H.; Tan, X.; Fan, Y.; Wei, L. A novel SOH estimation method with attentional feature fusion considering differential temperature features for lithium-ion batteries. *IEEE Trans. Instrum. Meas.* **2024**, *73*, 3538911. [CrossRef]
45. Zhao, H.; Chen, Z.; Shu, X.; Shen, J.; Lei, Z.; Zhang, Y. State of health estimation for lithium-ion batteries based on hybrid attention and deep learning. *Reliab. Eng. Syst. Saf.* **2023**, *232*, 109066. [CrossRef]
46. Sulaiman, M.H.; Mustaffa, Z.; Mohamed, A.I.; Samsudin, A.S.; Rashid, M.I.M. Battery state of charge estimation for electric vehicle using Kolmogorov-Arnold networks. *Energy* **2024**, *311*, 133417. [CrossRef]
47. Chen, C.; Wu, Y.; Shi, J.; Yue, D.; Shi, G.; Lyu, D. A parallel weighted ADTC-Transformer framework with FUnet fusion and KAN for improved lithium-ion battery SOH prediction. *Control Eng. Pract.* **2025**, *159*, 106302. [CrossRef]

Disclaimer/Publisher's Note: The statements, opinions and data contained in all publications are solely those of the individual author(s) and contributor(s) and not of MDPI and/or the editor(s). MDPI and/or the editor(s) disclaim responsibility for any injury to people or property resulting from any ideas, methods, instructions or products referred to in the content.